Supporting Information for "Water abundance of dunes in Gale crater, Mars from active neutron experiments & implications for amorphous phases"

Contents of this file

1. Text S1 to S1
2. Figures S1 to S6
3. Tables S1 to S3
4. References

Introduction This Supplementary Information includes two distinct materials: (1) a description of the data processing pipeline for active DAN measurements and (2) supporting figures and tables for the main manuscript. All data products for the DAN instrument used in the preparation of this manuscript are hosted publicly on the Planetary Data System (PDS) (www.pds.nasa.gov). Tools for preprocessing of binary data products to (raw) active DAN count data are also available as part of the PDS.

Text S1. Measured data from the CTN and CETN detectors, $\mathbf{D}^{\mathrm{CTN}}$ and $\mathbf{D}^{\mathrm{CETN}}$ respectively, are compared to those provided by MCNP6 models of the experiment, $\mathbf{M}^{\mathrm{CTN}}$ and $\mathbf{M}^{\mathrm{CETN}}$ respectively. Using the Monte Carlo N-Particle 6 (MCNP6) transfer code, the DAN active experiment will be modeled several times, each model will vary some aspect of the geochemistry of the martian subsurface. Often the hydrogen content will be varied, while all other elemental abundances and rover components are kept constant. The abundance of other major rock-forming elements are sourced from APXS experiments (see Table S1). A set of models, with variable hydrogen and other free parameters, are then compared to the measurement in order to find a 'best-fit' model [e.g. *Mitrofanov et al.*, 2014; *Sanin et al.*, 2015].

Unlike in the MCNP6 models for active DAN experiments, where the PNG is the only source of neutrons, the actual active DAN experiment on Mars is subject to background signal. This signal is due to both cosmic-ray bombardment that produces thermalized neutrons and the alpha decay of 238-plutonium from the Multi-Mission Radioisotope Thermoelectric Generator (MMRTG) which is the primary power source for the Curiosity Rover. This background signal is constant over the course of a ∼20-minute active DAN experiment and can be directly computed from neutron die-away curves by taking advantage of the design of the detector integration time [*Sanin et al.*, 2015]; after the decay of thermal neutrons returning from the subsurface after a single pulse, the detectors remain on for some time to detect the background signal. Although *Sanin et al.* [2015] describes the correction of background used herein, we outline these steps for completeness. Long after the peak arrival of thermalized neutrons, the DAN detectors continue integrating for a total time of 100,000 μs in 64 time bins. These late time bins can be used to compute a background count rate which can then be subtracted from the spectra [*Sanin et al.*, 2015]. Using the time bins from *Sanin et al.* [2015], b_i^{BG}=48 and b_f^{BG}=63 (counting from 1, with endpoints included), we first compute the total number of counts in late time bins in both detectors,

$$C_{\mathrm{BG}}^{\mathrm{CTN}} = \sum_{b_i^{\mathrm{BG}}}^{b_f^{\mathrm{BG}}} \mathbf{D}^{\mathrm{CTN}}$$
$$C_{\mathrm{BG}}^{\mathrm{CETN}} = \sum_{b_i^{\mathrm{BG}}}^{b_f^{\mathrm{BG}}} \mathbf{D}^{\mathrm{CETN}},$$

and divide the count number by the total elapsed time from bin 48 to 63, $\Delta t_{\mathrm{BG}} = 54278.7$ μs,

$$\dot{C}_{\mathrm{BG}}^{\mathrm{CTN}} = \frac{C_{\mathrm{BG}}^{\mathrm{CTN}}}{\Delta t_{\mathrm{BG}}}$$
$$\dot{C}_{\mathrm{BG}}^{\mathrm{CETN}} = \frac{C_{\mathrm{BG}}^{\mathrm{CETN}}}{\Delta t_{\mathrm{BG}}}.$$

The uncertainty in the background count rate is also computed,

$$\delta_{\mathrm{BG}}^{\mathrm{CTN}} = \frac{1}{\Delta t_{\mathrm{BG}}} \sqrt{\sum_{b_i^{\mathrm{BG}}}^{b_f^{\mathrm{BG}}} (\delta_{\mathbf{D}^{\mathrm{CTN}}})^2}$$
$$\delta_{\mathrm{BG}}^{\mathrm{CETN}} = \frac{1}{\Delta t_{\mathrm{BG}}} \sqrt{\sum_{b_i^{\mathrm{BG}}}^{b_f^{\mathrm{BG}}} (\delta_{\mathbf{D}^{\mathrm{CETN}}})^2},$$

where $\delta_{\mathbf{D}}$ is the 1σ uncertainty in the DAN count data $\mathbf{D}$. We assume the count data follows the Poisson distribution, *i.e.* $\delta_{\mathbf{D}} = \sqrt{\mathbf{D}}$.

Then the contribution of background is removed from each bin according to the background count rate for the particular detector and the time elapsed in each bin, *i.e.* the width of the corresponding time bin,

$$\mathbf{D}'^{\mathrm{CTN}} = \mathbf{D}^{\mathrm{CTN}} - \dot{C}_{\mathrm{BG}}^{\mathrm{CTN}} \Delta \mathbf{t}$$
$$\mathbf{D}'^{\mathrm{CETN}} = \mathbf{D}^{\mathrm{CETN}} - \dot{C}_{\mathrm{BG}}^{\mathrm{CETN}} \Delta \mathbf{t}.$$

The uncertainty in this computation is also propagated for each time bin,

$$\delta'_{\mathbf{D}^{\mathrm{CTN}}} = \sqrt{(\delta_{\mathbf{D}^{\mathrm{CTN}}})^2 + (\delta_{\mathrm{BG}}^{\mathrm{CTN}} \Delta \mathbf{t})^2}$$
$$\delta'_{\mathbf{D}^{\mathrm{CETN}}} = \sqrt{(\delta_{\mathbf{D}^{\mathrm{CETN}}})^2 + (\delta_{\mathrm{BG}}^{\mathrm{CETN}} \Delta \mathbf{t})^2}$$

and the effect of background subtraction is demonstrated in Figure S2.

Since the overall shape of neutron die-away curves are indicative of subsurface geochemistry [*Hardgrove et al.*, 2011] we compare the shape of die-away curves for the time bins that demonstrate the most dynamic range with respect to changing subsurface geochemistry [*Sanin et al.*, 2015]. The time bins used herein are similar to those in *Sanin et al.* [2015], b_i^{CTN}=18 and b_f^{CTN}=34 in the CTN detector, and b_i^{CETN}=13 and b_f^{CETN}=17 in the CETN detector (counting

0094-8276/18/$5.00

from 1). We first normalize the MCNP6 count tally data to that of the DAN data in the time bins of interest, effectively translating the model tally data into count space. First, we compute a sum of the detector data separately for both detectors,

$$U^{\mathrm{CTN}} = \sum_{b_i^{\mathrm{CTN}}}^{b_f^{\mathrm{CTN}}} \mathbf{D}'^{\mathrm{CTN}}$$
$$U^{\mathrm{CETN}} = \sum_{b_i^{\mathrm{CETN}}}^{b_f^{\mathrm{CETN}}} \mathbf{D}'^{\mathrm{CETN}}.$$

The uncertainty of the sum is also computed,

$$\delta_{U^{\mathrm{CTN}}} = \sqrt{\sum_{b_i^{\mathrm{CTN}}}^{b_f^{\mathrm{CTN}}} \left(\delta'_{\mathbf{D}^{\mathrm{CTN}}}\right)^2}$$
$$\delta_{U^{\mathrm{CETN}}} = \sqrt{\sum_{b_i^{\mathrm{CETN}}}^{b_f^{\mathrm{CETN}}} \left(\delta'_{\mathbf{D}^{\mathrm{CETN}}}\right)^2}.$$

Then, we compute the same sum of the *model* data, separately for both detectors,

$$V^{\mathrm{CTN}} = \sum_{b_i^{\mathrm{CTN}}}^{b_f^{\mathrm{CTN}}} \mathbf{M}^{\mathrm{CTN}}$$
$$V^{\mathrm{CETN}} = \sum_{b_i^{\mathrm{CETN}}}^{b_f^{\mathrm{CETN}}} \mathbf{M}^{\mathrm{CETN}}.$$

The uncertainty of the sum is also computed,

$$\delta_{V^{\mathrm{CTN}}} = \sqrt{\sum_{b_i^{\mathrm{CTN}}}^{b_f^{\mathrm{CTN}}} \left(\delta_{\mathbf{M}^{\mathrm{CTN}}}\right)^2}$$
$$\delta_{V^{\mathrm{CETN}}} = \sqrt{\sum_{b_i^{\mathrm{CETN}}}^{b_f^{\mathrm{CETN}}} \left(\delta_{\mathbf{M}^{\mathrm{CETN}}}\right)^2}.$$

By dividing both sums, U and V, we arrive at the conversion factor X that converts tally data to count space,

$$X^{\mathrm{CTN}} = \frac{U^{\mathrm{CTN}}}{V^{\mathrm{CTN}}},$$
$$X^{\mathrm{CETN}} = \frac{U^{\mathrm{CETN}}}{V^{\mathrm{CETN}}},$$

with error propagated as such:

$$\delta_{X^{\mathrm{CTN}}} = \frac{U^{\mathrm{CTN}}}{V^{\mathrm{CTN}}} \sqrt{\left(\frac{\delta_{U^{\mathrm{CTN}}}}{U^{\mathrm{CTN}}}\right)^2 + \left(\frac{\delta_{V^{\mathrm{CTN}}}}{V^{\mathrm{CTN}}}\right)^2}$$
$$\delta_{X^{\mathrm{CETN}}} = \frac{U^{\mathrm{CETN}}}{V^{\mathrm{CETN}}} \sqrt{\left(\frac{\delta_{U^{\mathrm{CETN}}}}{U^{\mathrm{CETN}}}\right)^2 + \left(\frac{\delta_{V^{\mathrm{CETN}}}}{V^{\mathrm{CETN}}}\right)^2}.$$

Then the tally data from MCNP6 models are normalized,

$$\mathbf{M}'^{\mathrm{CTN}} = \mathbf{M}^{\mathrm{CTN}} X^{\mathrm{CTN}}$$
$$\mathbf{M}'^{\mathrm{CETN}} = \mathbf{M}^{\mathrm{CETN}} X^{\mathrm{CETN}}$$

and the error is propagated,

$$\delta'^{\mathrm{CTN}}_{\mathbf{M}} = \mathbf{M}^{\mathrm{CTN}} X^{\mathrm{CTN}} \sqrt{\left(\frac{\delta_{\mathbf{M}^{\mathrm{CTN}}}}{\mathbf{M}^{\mathrm{CTN}}}\right)^2 + \left(\frac{\delta_{X^{\mathrm{CTN}}}}{X^{\mathrm{CTN}}}\right)^2}$$
$$\delta'^{\mathrm{CETN}}_{\mathbf{M}} = \mathbf{M}^{\mathrm{CETN}} X^{\mathrm{CETN}} \sqrt{\left(\frac{\delta_{\mathbf{M}^{\mathrm{CETN}}}}{\mathbf{M}^{\mathrm{CETN}}}\right)^2 + \left(\frac{\delta_{X^{\mathrm{CETN}}}}{X^{\mathrm{CETN}}}\right)^2}.$$

At this point, the normalized model data, $\mathbf{M}'$, can be compared to background subtracted data, $\mathbf{D}'$, from an active DAN experiment.

Instead of minimizing the χ^2 parameter as a means of finding a best-fit model, as is performed in *Mitrofanov et al.* [2014]; *Sanin et al.* [2015], we employ a Markov Chain Monte Carlo (MCMC) method [*Foreman-Mackey et al.*, 2013] to maximize the likelihood function, or more specifically minimize the negative log of the likelihood function:

$$\mathcal{L} = -\frac{1}{2} \sum_i^N \left(\frac{(C_i - \mathcal{M}_i(p_0, p_1, ..., p_N)}{\sigma_i^2} + ln(2\pi\sigma_i^2) \right),$$

where C_i is the measurement data, $\mathcal{M}_i$ an interpolant of the modeled data as a function of the free parameters, *e.g.* H abundance, and the sum is taken over the range of time bins in the CTN detector shown in Figure S3. We have found that the CETN detector is not diagnostic, *i.e.* lacks dynamic range over the parameters of this study, and thus it is excluded from this analysis. The variance of the data and the model in each time bin is captured by the σ_i^2 term,

$$\sigma_i^2 = \delta C_i^2 + \delta \mathcal{M}_i^2(p_0, p_1, ..., p_N) + f^2,$$

where δC_i is the uncertainty of DAN data and $\delta\mathcal{M}_i$ is the uncertainty in the modeled spectra. Our MCNP6 models simulate 2.5e9 particles which provides <<5% relative error in modeled spectra for the time bins of interest. We conservatively set $\delta\mathcal{M}_i$ to be a constant 5% relative error. A new free parameter has been introduced, f, which represents the underestimation of the count uncertainty. Larger values of this parameter indicate either poor statistical convergence in the model, poor statistical convergence in the measurement, and/or a poor overall fit of the model to the data, *i.e.* inaccurate model assumptions; however, in our study we find reasonable values of f, *i.e.* f is less than a few percent of the counts in DAN spectra. In sum, the MCMC routine will find the combination of hydrogen abundance and other free parameters, *e.g.* depth, that best fits the observed spectra, while also accounting for underestimated uncertainties.

The computational resources to generate a synthetic model of active DAN spectra using the MCNP6 code is not insignificant, on the order of several hours per model on ∼100 core compute clusters and on the order of days on modern desktops. Thus the generation of model data cannot occur 'in line' with the MCMC routine, but rather a 'grid' of models are generated beforehand. A model grid is composed of models that vary the free parameters, $p_0, p_1, ..., p_N$, to discrete values for which we are trying to find a non-discrete 'best-fit' value of the free parameters. In the case of DAN, examples of free parameters include hydrogen content, depth of a geochemically-distinct top layer, bulk density, etc. In the analysis to determine the water content of the local (Murray formation) bedrock performed herein, we allowed only hydrogen content to vary, from 1 WEH to 6 WEH in increments of 0.2 WEH.

Once a model grid is simulated, an interpolant is generated, $\mathcal{M}(p_0, p_1, ..., p_N)$, which allows the MCMC routine

to produce modeled active DAN spectra at non-discrete parameter values. We choose to employ a linear interpolant, which assumes the behavior of the count rate as a function of the free parameter is linear, for a given bin, between discrete increments of the parameters. This assumption is appropriate when the free parameters have sufficient resolution; we find a resolution of 0.2-0.4 WEH is an appropriate sampling resolution for bulk water content and 5-10 cm is an appropriate sampling resolution for depth.

Before comparing the model grid to data, the MCMC routine requires an *a priori* 'guess' of the free parameters for each walker. We found the results of this study are rather insensitive to the initial conditions, provided the MCMC routine is allowed sufficient iterations. The *a priori* (mean and 1 standard deviation) for the water content of the bedrock in the homogeneous model was 3.0 ± 0.3 WEH. For the two-layer models, the *a priori* for the dune hydrogen was 1.0 ± 0.3 WEH and the *a priori* for the depth was 40 ± 10 cm. In both cases the *a priori* for the parameter f was 40 ± 10 counts. We simulated $8N_p$ walkers, where N_p is the number of free parameters; $N_p = 1$ in the case of the bedrock model analysis (variable hydrogen in a single layer) and $N_p = 2$ in the case of the dune analysis (variable hydrogen in the top layer, variable thickness of the top layer). We allowed the walkers to perform 10,000 steps (iterations) in the parameter space before the routine is halted. The mean and standard deviation of the free parameters are determined using the last 9,000 positions of each of the $8N_p$ walkers. The *a posteriori* distribution of the free parameters, which is composed of the 9,000 walker positions, is shown in a series of projections in Figures 1 and S4.

Table S1: Shown are the H-free elemental abundances[a] in wt% for drill targets. Values were converted from oxide abundances provided by APXS experiments of drill tailing piles. The last row shows that the geochemistry of active dune sands are within 2 standard deviations in macroscopic absorption cross section, resulting in similar signatures in DAN spectra. To compute the uncertainty on $\xi_{\rm abs}$ we assumed no uncertainty on $\sigma_{\rm abs}$ and used (1σ) oxide uncertainties from APXS data products[b]. Compositions were renormalized to include the water content of the simulation.

	Drill Sites			
Element	*Sebina*	*Gobabeb* Dump Pile B	*Ogunquit Beach*	$\sigma_{\rm abs}$ [barns][b]
Cl	1.06	0.498	0.530	33.5
Mn	0.124	0.333	0.318	13.3
Br	0.0104	0.00810	0.00310	6.90
Ti	0.659	0.408	0.558	6.10
Ni	0.102	0.0696	0.0488	4.49
Cr	0.205	0.166	0.349	3.05
Fe	14.2	15.4	15.3	2.56
K	0.689	0.334	0.382	2.10
Zn	0.0814	0.0152	0.0241	1.11
Na	1.49	1.28	1.91	0.53
S	3.66	1.17	1.38	0.53
Ca	5.10	4.77	5.15	0.43
Al	4.59	4.17	4.98	0.231
P	0.266	0.343	0.327	0.172
Si	21.6	21.6	21.1	0.171
Mg	2.56	6.93	5.30	0.063
O (remainder)[c]	43.6	42.5	42.340	0.00019
$\xi_{\rm abs} \pm 1\sigma$ [barns][d]	0.902 ± 0.011	0.731 ± 0.015	0.757 ± 0.009	

[a] Isotopic abundances of each element, required for the MCNP6 input file, are computed assuming terrestrial abundances [*Berglund and Wieser*, 2011].

[b] $\sigma_{\rm abs}$ is the absorption cross section of an element (assuming terrestrial isotopic abundances) and is provided by *Sears* [1992] for 2,200 m/s neutrons.

[c] Since APXS provides all major rock-forming elements, we assume the remaining species is oxygen.

[d] The macroscopic absorption cross section, $\xi_{\rm abs} = \sigma_{\rm abs,i} a_{\rm i} / \Sigma_i a_i$, is a measure of a rock's ability to suppress thermal neutrons. Values of $\xi_{\rm abs}$ can thus be used to discern whether rocks will have similar neutron spectra for a constant H content.

Table S2: Shown are the amorphous phases used in the modeling herein and their associated geochemical abundances in wt%. The chemical formula represents the dehydrated form of each phase from which the water-free abundances were computed. The abundances of each phase are renormalized to account for the water content listed in the last column.

Amorphous phase	Formula	SiO_2	TiO_2	Al_2O_3	FeO_T	MnO	MgO	CaO	Na_2O	K_2O	P_2O_5	SO_3	H_2O
Basaltic glass[a]	N/A	46.91	0.56	10.92	19.21	0.42	10.64	8.01	2.56	0.10	0.57	-	0.10[c]
Rhyolitic glass[b]	N/A	71.06	0.30	16.87	1.02	-	-	0.34	8.38	1.94	-	-	0.10[c]
Opal	SiO_2	98.50	-	-	-	-	-	-	-	-	-	-	2.0[d]
Ca phosphate	$Ca_3(PO_4)_2$	-	-	-	-	-	-	54.24	-	-	45.76	-	-
K sulfate	K_2SO_4	-	-	-	-	-	-	-	-	54.06	-	45.94	-
Na sulfate	Na_2SO_4	-	-	-	-	-	-	-	43.64	-	-	56.36	-
Fe sulfate	$Fe_2(SO_4)_3$	-	-	-	31.44	-	-	-	-	-	-	47.29	21.27
Mg sulfate	$MgSO_4$	-	-	-	-	-	26.12	-	-	-	-	51.88	22.00
Allophane	$Al_2O_3(SiO_2)_{1.5}$	49.63	-	43.87	-	-	-	-	-	-	-	-	6.50[e]
Hisingerite	$Fe_2O_3SiO_2$	26.63	-	-	70.77	-	-	-	-	-	-	-	2.60[f]
Ferrihydrite	Fe_2O_3	-	-	-	96.00	-	-	-	-	-	-	-	4.00[e]

[a] Water-free abundances sourced from *Filiberto et al.* [2008] [b] Water-free abundances sourced from *Varela et al.* [2000] [c] Water abundance sourced from *Filiberto and Treiman* [2009] that estimated parent magmas of martian meteorites to have <0.3 wt% H_2O [d] Water abundance computed from bulk water content reported by *in situ* EGA experiments of primarily opaline material in Gale crater [*Rapin et al.*, 2018] [e] Water abundance sourced from *Rampe et al.* [2016] [f] Water abundance sourced from follow-on experiments from *Rampe et al.* [2016]

Table S3: Shown are the Cl- and Cr-free oxide abundances estimated for the amorphous component of the *Ogunquit Beach* sand[a]. Compositions were calculated for the minimum, 33 wt%, and maximum, 55 wt%, esimates of the X-ray amorphous material in the sample [*Rampe et al.*, 2018]. Deriving geochemical abundances for the amorphous fraction requires assumptions about the geochemistry of crystalline phases, *e.g.* assuming an Mg content of pyroxene, and an assumption on the amorphous fraction, *e.g.* assuming amorphous material composes 33 wt% of the bulk [e.g. *Rampe et al.*, 2018]. However, we do not attempt to address the effects of varying the former, but reserve that for future study. As such, the range of abundances reported in the table represent the minimum range of oxide abundances. To account for this, 'good fit' models fall within 2 times the range of the oxides reported for the minimum and maximum amorphous fraction assumptions (*e.g.*, the SiO_2 range is 43.58 wt% – 49.63 wt%). These constraints are not applied to Mn and Ti since olivine and pyroxene compositions, reported as Fe-Mg and Fe-Mg-Ca solid solutions in *Rampe et al.* [2018], do not account for the presence of trace elements possible in the mineral structures. Furthermore, minerals in abundance of <1 wt% are below the CheMin instrument detection limit. Thus, trace elements in major crystalline phases and those comprising undetectable crystalline phases are included in the calculated amorphous composition.

	Amorphous fraction	
Oxide	33 %	55 %
SiO_2	**46.00**	47.21
TiO_2	2.90	**1.73**
Al_2O_3	**5.10**	8.38
FeO	25.80	**20.86**
MnO	1.12	**0.67**
MgO	**0.00**	4.58
CaO	**4.06**	5.96
Na_2O	3.02	**2.94**
K_2O	1.84	**1.09**
P_2O_5	2.37	**1.41**
SO_3	7.78	**5.18**

[a] Crystalline phase compositions are reported in [*Rampe et al.*, 2018].

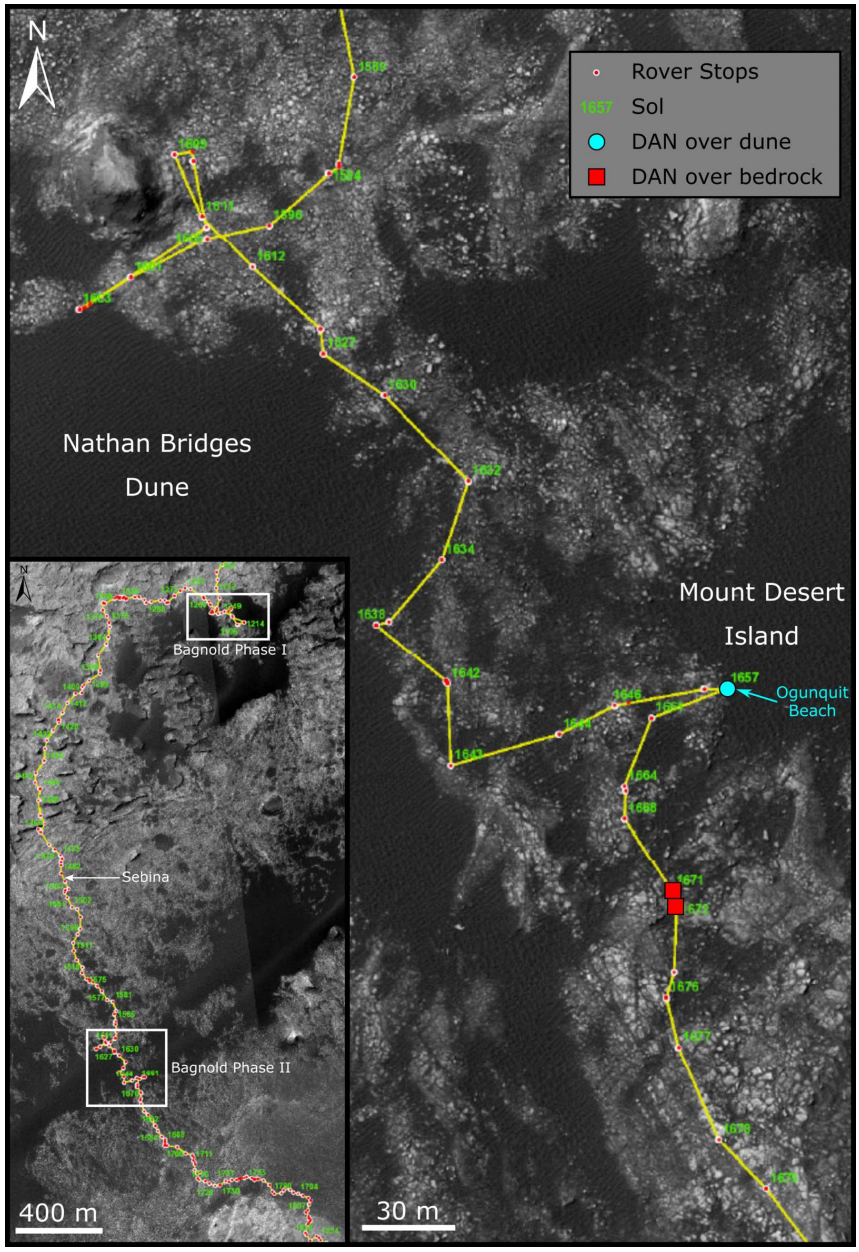

Figure S1: Shown is a map of the Bagnold campaign; dark material is part of the larger Bagnold Dunes. The active DAN dune measurement at Mount Desert Island is shown as a blue circle; this is the location of the *Ogunquit Beach* target. Locations of DAN measurements used to determine the water abundance of the local bedrock are shown as red squares. The inset shows phase 1 in context with phase 2 and the *Sebina* drill target. Rover stops and associated sols are shown as red circles and green text respectively.

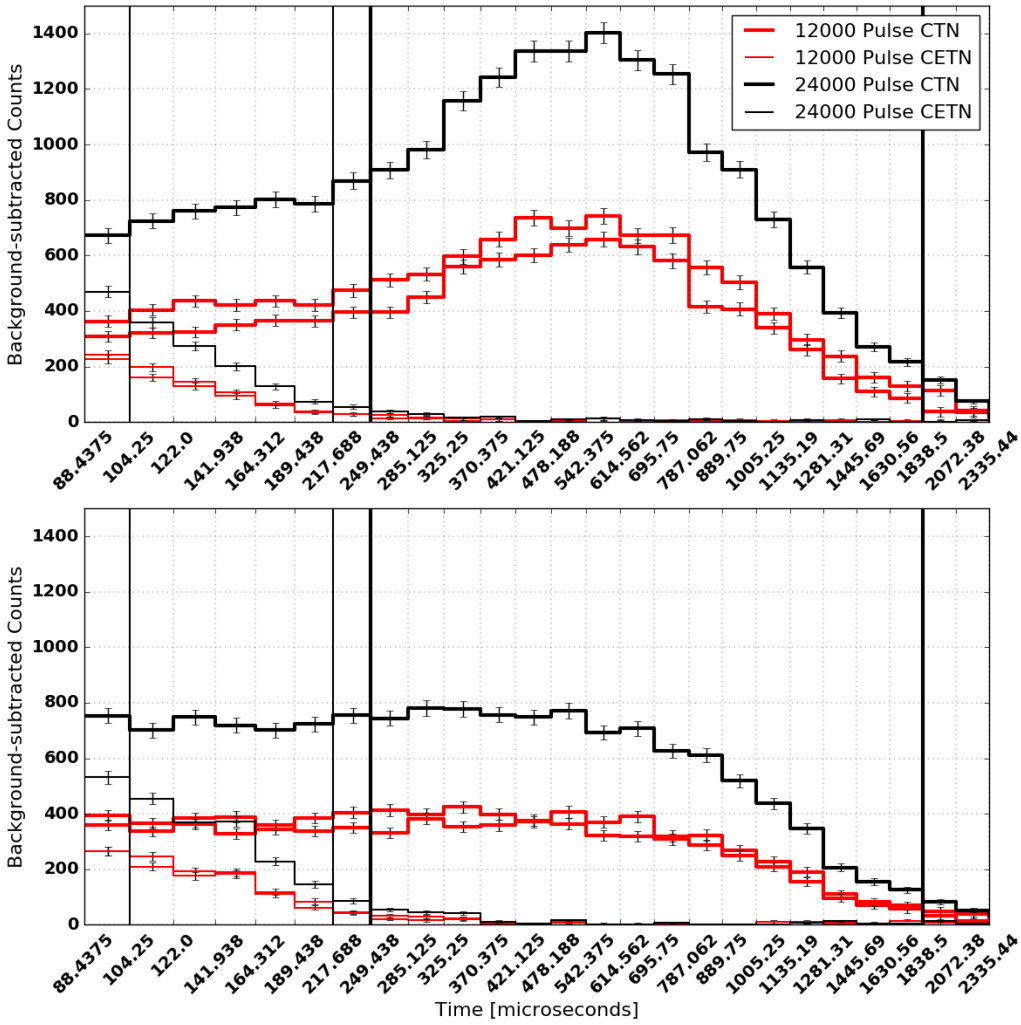

Figure S2: Shown are plots of background-subtracted active DAN data. Thin and thick lines represent data from the CETN and CTN detector, respectively. (Top) Neutron die-away curves from bedrock measurements at the same location on sols 1669 and 1671 (red lines) were coadded to produce a more statistically converged curve (black lines). (Bottom) The same coadding process was performed for the two dune measurements at Mount Desert Island on sol 1659. The peak of thermal neutrons in the CTN detector for the off-dune measurement (top) is not featured in the on-dune measurement (bottom), indicating the on-dune measurement detected less H. The thin and thick vertical lines mark the bounds of the time bin ranges used in data-to-model comparative analyses of the CETN and CTN detectors, respectively.

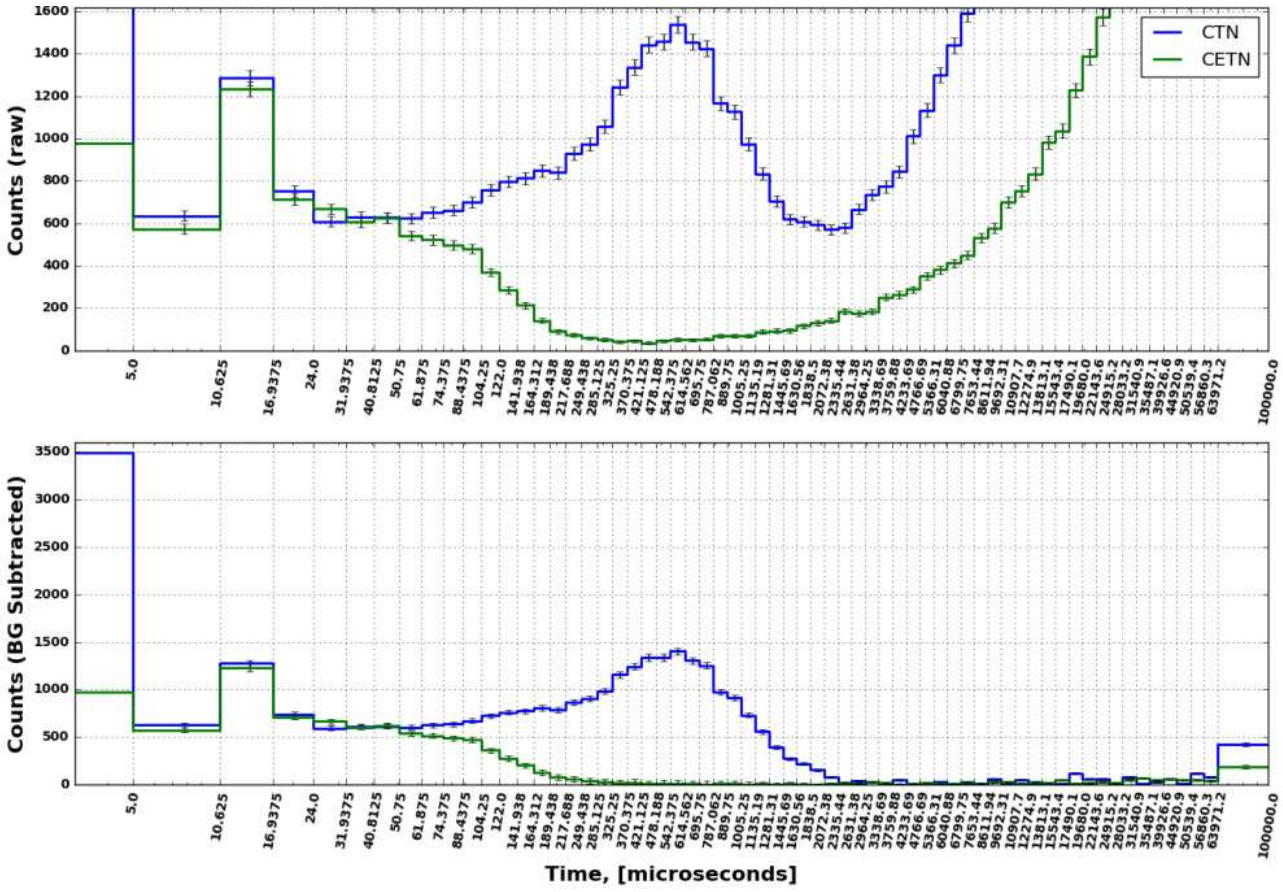

Figure S3: Shown are raw DAN die-away data (top) and background subtracted die-away data (bottom) for the coadded data from sol 1669 and 1671. Early-arriving neutrons are directly scattered from the rover body and are not diagnostic of subsurface geochemistry [*Mitrofanov et al.*, 2014; *Sanin et al.*, 2015]. Late-arriving neutrons are successfully removed through the background subtraction procedure (bottom).

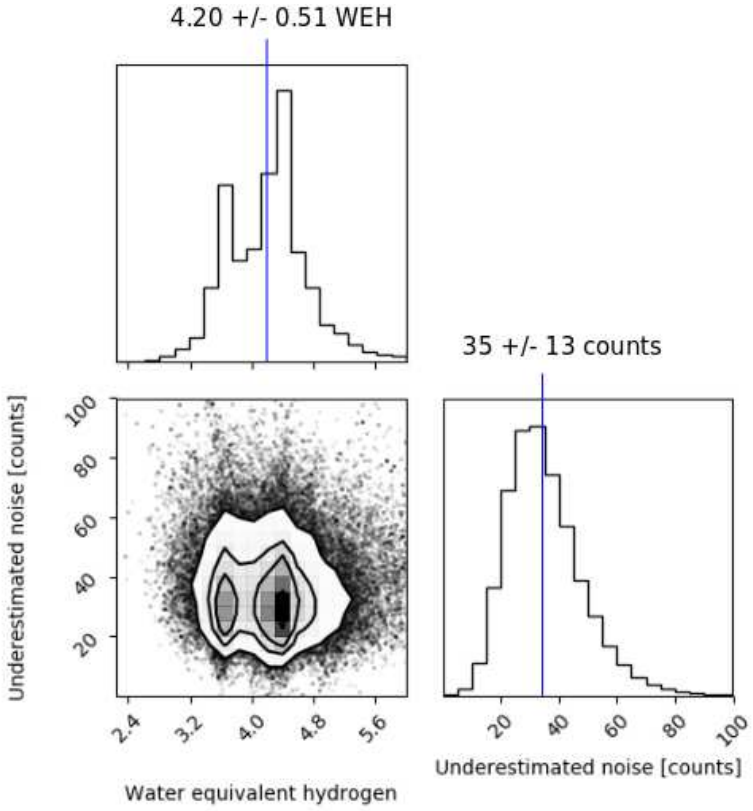

Figure S4: Shown are the *a posteriori* distributions of the fitted parameters determined from models of a homogeneous *Sebina* (Murray) composition. The marginalized distributions are projected as histograms along the diagonal. The mean and standard deviation of the hydrogen content is 4.20 ± 0.51 WEH and f=35 ± 13 counts, with a correlation coefficient of 0.03 between the two parameters.

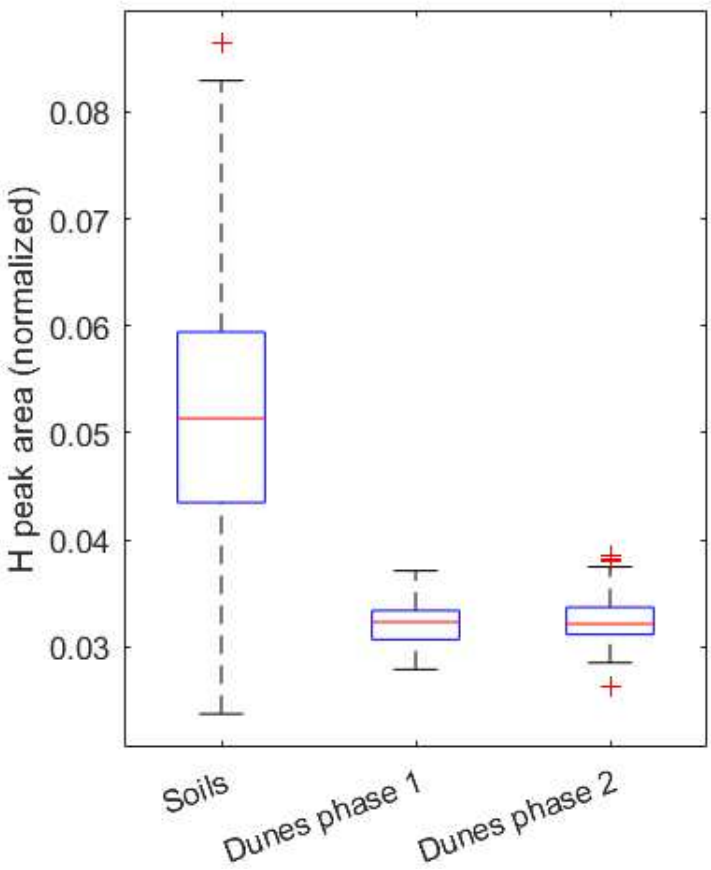

Figure S5: Distribution of the ChemCam hydrogen peak area (Normalized to O peak area at 778 nm) [*Rapin et al.*, 2017] for the soils and dune materials. Soils refers fine-grained soils analyzed using the "blind target mode" [*Cousin et al.*, 2017]. Dunes phase 1 and phase 2 correspond to all Laser Induced Breakdown Spectroscopy data obtained on Bagnold Dune sand in the phase 1 and phase 2 campaigns. Due to a number of points obtained with a poor laser focus, a threshold was applied to remove spectra with low intensity. *Cousin et al.* [2017] showed similar results on the hydrogen signal using the hydrogen ICA score [*Forni et al.*, 2013] and here we extend the result to the Bagnold Dunes phase 2 measurements using the hydrogen peak fitting method.

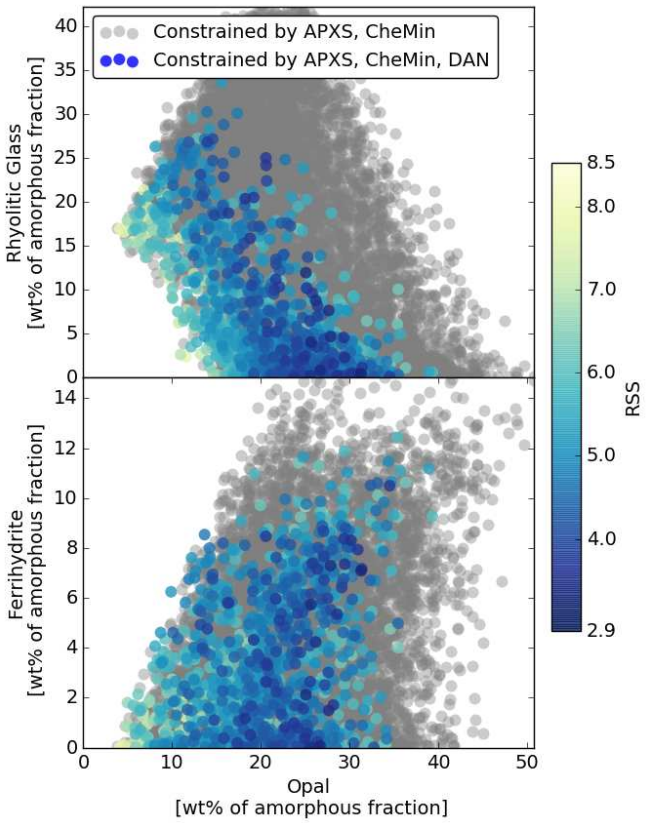

Figure S6: Shown are abundances of opal and rhyolitic glass (top), as well as opal and ferrihydrite (bottom) for the 10,000 amorphous composition models shown in Figure 2. Grey points represent models that do not fit the DAN-derived water abundance of the amorphous fraction and colored points represent models that fit all constraints. Opal and rhyolitic glass are shown to be anticorrelated whereas opal and ferrihydrite are correlated.

References

Berglund, M., M. E. Wieser (2011), Isotopic compositions of the elements 2009 (IUPAC Technical Report), *Pure and Applied Chemistry*, *83*(2), 397–410,doi:10.1351/PAC-REP-10-06-02.

Cousin, A., E. Dehouck, P.-Y. Meslin, O. Forni, A. J. Williams, N. Stein, O. Gasnault, N. Bridges, B. Ehlmann, S. Schröder, V. Payré, W. Rapin, P. Pinet, V. Sautter, N. Lanza, J. Lasue, S. Maurice, and R. C. Wiens (2017), Geochemistry of the Bagnold dune field as observed by ChemCam and comparison with other aeolian deposits at Gale Crater, *Journal of Geophysical Research: Planets*, *122*(10), 2144–2162, doi:10.1002/2017JE005261.

Filiberto, J., and A. H. Treiman (2009), Martian magmas contained abundant chlorine, but little water, *Geology*, *37*(12), 1087–1090, doi:10.1130/G30488A.1.

Filiberto, J., A. H. Treiman, and L. Le (2008), Crystallization experiments on a Gusev Adirondack basalt composition, *Meteoritics and Planetary Science*, *43*(7), 1137–1146, doi:10.1111/j.1945-5100.2008.tb01118.x.

Foreman-Mackey, D., D. W. Hogg, D. Lang, and J. Goodman (2013), emcee: The MCMC Hammer, *Publ. A. S. P.,* , *125*(925), 306–312, doi:10.1086/670067.

Forni, O., S. Maurice, O. Gasnault, R. C. Wiens, A. Cousin, S. M. Clegg, J. B. Sirven, and J. Lasue (2013), Independent component analysis classification of laser induced breakdown spectroscopy spectra, *Spectrochimica Acta Part B: Atomic Spectroscopy*, *86*, 31–41, doi:10.1016/j.sab.2013.05.003.

Hardgrove, C., J. Moersch, and D. Drake (2011), Effects of geochemical composition on neutron die-away measurements: Implications for Mars Science Laboratory's Dynamic Albedo of Neutrons experiment, *Nuclear Instruments and Methods in Physics Research, Section A: Accelerators, Spectrometers, Detectors and Associated Equipment*, *659*(1), 442–455, doi:10.1016/j.nima.2011.08.058.

Mitrofanov, I. G., M. L. Litvak, A. B. Sanin, R. D. Starr, D. I. Lisov, R. O. Kuzmin, A. Behar, W. V. Boynton, C. Hardgrove, K. Harshman, I. Jun, R. E. Milliken, M. A. Mischna, J. E. Moersch, and C. G. Tate (2014), Water and chlorine content in the Martian soil along the first 1900 m of the Curiosity rover traverse as estimated by the DAN instrument, *Journal of Geophysical Research: Planets*, *119*(7), 1579–1596, doi:10.1002/2013JE004553.

Rampe, E. B., R. V. Morris, P. D. Archer, Jr, D. G. Agresti, and D. W. Ming (2016), Recognizing sulfate and phosphate complexes chemisorbed onto nanophase weathering products on mars using in-situ and remote observations, *American Mineralogist*, *101*(3), 678–689, doi:10.2138/am-2016-5408CCBYNCND.

Rampe, E. B., M. Lapotre, T. F. Bristow, R. E. Arvidson, R. V. Morris, C. N. Achilles, C. Weitz, D. F. Blake, D. W. Ming, S. M. Morrison, D. T. Vaniman, S. J. Chipera, R. T. Downs, J. P. Grotzinger, R. M. Hazen, T. S. Peretyazhko, B. Sutter, V. Tu, A. S. Yen, B. Horgan, N. Castle, P. I. Craig, D. J. Des Marais, J. Farmer, R. Gellert, A. C. McAdam, J. M. Morookian, P. C. Sarrazin, and A. H. Treiman (2018), Sand mineralogy within the Bagnold Dunes, Gale crater, as observed in situ and from orbit, *Journal of Geophysical Research: Planets*, *45*(18), 9488–9497.

Rapin, W., P.-Y. Meslin, S. Maurice, R. Wiens, D. Laporte, B. Chauvir, O. Gasnault, S. Schroder, P. Beck, S. Bender, O. Beyssac, A. Cousin, E. Dehouck, C. Drouet, O. Forni, M. Nachon, N. Melikechi, B. Rondeau, N. Mangold, and N. Thomas (2017), Quantification of water content by laser induced breakdown spectroscopy on mars, *Spectrochimica Acta Part B: Atomic Spectroscopy*, *130*, 82–100, doi:https://doi.org/10.1016/j.sab.2017.02.007.

Rapin, W., B. Chauvire, T. S. J. Gabriel, A. C. McAdam, B. Ehlmann, C. Hardgrove, P.-Y. Meslin, B. Rondeau, E. Dehouck, H. B. Franz, N. Mangold, S. J. Chipera, R. C. Wiens, J. Frydenvang, and S. Schroder (2018), In situ analysis of opal in Gale crater, Mars, *Journal of Geophysical Research: Planets*, *23*(8), 1955–1972 doi:10.1029/2017JE005483.

Sanin, A. B., I. G. Mitrofanov, M. L. Litvak, D. I. Lisov, R. Starr, W. Boynton, A. Behar, L. DeFlores, F. Fedosov, D. Golovin, C. Hardgrove, K. Harshman, I. Jun, A. S. Kozyrev, R. O. Kuzmin, A. Malakhov, R. Milliken, M. Mischna, J. Moersch, M. I. Mokrousov, S. Nikiforov, V. N. Shvetsov, C. Tate, V. I. Tret'Yakov, and A. Vostrukhin (2015), Data processing of the active neutron experiment DAN for a Martian regolith investigation, *Nuclear Instruments and Methods in Physics Research, Section A: Accelerators, Spectrometers, Detectors and Associated Equipment*, *789*, 114–127, doi:10.1016/j.nima.2015.03.085.

Sears, V. F. (1992), Neutron scattering lengths and cross sections, *Neutron News*, *3*(3), 26–37, doi:10.1080/10448639208218770.

Varela, M. E., G. Kurat, M. Bonnin-Mosbah, R. Clocchiatti, and D. Massare (2000), Glass-bearing inclusions in olivine of the Chassigny achondrite: Heterogeneous trapping at sub-igneous temperatures, *Meteoritics and Planetary Science*, *35*(1), 39–52, doi:10.1111/j.1945-5100.2000.tb01972.x.

Corresponding author: T.S.J. Gabriel, School of Earth and Space Exploration, Arizona State University, ISTB4, Tempe, AZ 85287-6004, USA. (travis.gabriel@asu.edu)